batteries

MDPI

Article

Low Voltage Charge/Discharge Behavior of Manganese Hexacyanoferrate

Takayuki Shibata [1,2], Masamitsu Takachi [3] and Yutaka Moritomo [1,3,4,*]

1 Faculty of Pure and Applied Science, University of Tsukuba, Tsukuba 305-8571, Japan; shibata@nat.gunma-ct.ac.jp
2 Department of Physics, National Institute of Technology, Gunma College, Toriba-cho, Maebashi-Shi, Gunma 371-8530, Japan
3 Graduate School of Pure and Applied Science, University of Tsukuba, Tsukuba 305-8571, Japan; s1430088@u.tsukuba.ac.jp
4 Tsukuba Research Center for Interdisciplinary Materials Science (TIMS), University of Tsukuba, Tsukuba 305-8571, Japan
* Correspondence: moritomo.yutaka.gf@u.tsukuba.ac.jp; Tel.: +81-29-853-4337

Academic Editor: Andreas Jossen
Received: 27 January 2017; Accepted: 7 March 2017; Published: 10 March 2017

Abstract: Recently, Prussian blue analogues (PBAs) have been reported to exhibit a low voltage charge/discharge behavior with high capacity (300–545 mAh/g) in lithium-ion secondary batteries (LIBs). To clarify the mechanism of low voltage behavior, we performed ex situ synchrotron radiation X-ray diffraction (XRD) and ex situ X-ray absorption spectroscopy (XAS) of a film of $Na_{1.34}Mn[Fe(CN)_6]_{0.84}\cdot 3.4H_2O$ without air exposure. After the 1st discharge process, the XRD patterns and X-ray absorption spectra around the Fe and Mn K edges reveal formation of Fe and Mn metals. After the charge process, the XRD pattern reveals formation of Fe_2O_3. Based on these observations, we ascribed the low voltage behavior mainly to the conversion reaction of Fe_2O_3: $6e^- + Fe_2O_3 + 6Li^+ \rightleftharpoons 2Fe + 3Li_2O$.

Keywords: secondary battery; anode material; Prussian blue analogues; conversion reaction

1. Introduction

Nanoporous materials [1] have been attracting increasing interest due to their functionalities for lithium-ion secondary batteries (LIBs), hydrogen storage, molecular storage, and gas separation. Among nanoporous materials, transition metal hexacyanoferrates or Prussian blue and its analogues (PBAs), denoted as $A_xM[Fe(CN)_6]_y$ (A and M, are the alkali and transition metals, respectively), are most intensively investigated for LIBs [2–8] and sodium-ion secondary batteries (SIBs) [9–13]. The PBAs consist of three-dimensional cyano-bridged networks (jungle-gym type networks) of the transition metal, –M–NC–Fe–CN–M–, with periodic nano-cubes of 5 Å on each side [14,15]. Thin films of $Li_{1.32}Mn[Fe(CN)_6]_{0.83}\cdot 3.5H_2O$ show a high capacity of 128 mAh/g, good cyclability and an average operating voltage of 3.6 V against Li/Li^+ [5]. Goodenough's group [7] reported charge/discharge properties of the SIB cathodes in a K–M–$Fe(CN)_6$ system (M = Mn, Fe, Co, Ni, Cu, Zn) even though their coulomb efficiency is poor. The coulomb efficiency is significantly improved in thin films of $Na_{1.32}Mn[Fe(CN)_6]_{0.83}\cdot 3.5H_2O$ [8], and $Na_{1.6}Co[Fe(CN)_6]_{0.9}\cdot 2.9H_2O$ [9]. They show high capacities of 109 and 135 mAh/g and average operating voltages of 3.4 and 3.6 V against Na/Na^+, respectively.

Recently, PBAs have been reported to show reversible low voltage charge/discharge behavior with high capacity (300–545 mAh/g) in LIBs [16–20]. Shokouhimehr et al. [16] demonstrated that the Co-PBA nanoparticles show a reversible capacity of 544 mAh/g in the 0.01–3.0 V range against Li/Li^+ at current density of 100 mA/g. Nie et al. [17] investigated the anode performance

of $Co_3^{2+}[Co^{3+}(CN)_6]_2 \cdot nH_2O$ and $Mn_3^{2+}[Co^{3+}(CN)_6]_2 \cdot nH_2O$. They found that $Co_3^{2+}[Co^{3+}(CN)_6]_2$ exhibits a reversible capacity of 300 mAh/g in the 0.01–3.0 V range against Li/Li^+. They ascribed the behavior to the redox process of Co^{3+}/Co^{2+} and Co^{2+}/Co^+. Xiong et al. [18] reported that $Mn^{2+}[Fe^{3+}(CN)_6]_{2/3} \cdot nH_2O$ shows a reversible capacity of 296 mAh/g and average voltage of 0.5 V with good cyclability. They ascribed the behavior to the redox process of Fe^{3+}/Fe^{2+}. On the other hand, Piernas-Muñoz et al. [19] reported that $K_{0.88}Fe_{1.04}[Fe(CN)_6] \cdot yH_2O$ shows a reversible capacity of 400 mAh/g in the 0.005–1.6 V range against Li/Li^+. Based on the scanning electron microscopy (SEM) and transmission electron microscopy (TEM) observation, they tentatively ascribed the behavior to a conversion reaction: $K_{1-x}Fe^{III}{}_{1+x/3}[Fe^{II}(CN)_6] \cdot yH_2O + (5+x)Li^+ + (5+x)e^- \rightarrow (2+x/3)Fe + (5+x)LiZ + (1-x)KZ$ ($Z = CN^-, OH^-, F^-, ...$). Sun et al. [20] reported that $Ti_{0.75}Fe_{0.25}[Fe(CN)_6]_{0.96} \cdot 1.9H_2O$ shows a reversible capacity of 350 mAh/g in the 0–3.0 V range against Li/Li^+ with good cyclability and rate performance. They found that the X-ray diffraction (XRD) patterns of PBA electrode disappeared after discharge, and then the XRD patterns of PBA electrode did not appear after charging. Therefore, they ascribed the behavior to a conversion reaction: $Ti_x[Fe_{2-x}(CN)_6] \cdot 2H_2O + 6Li^+ + 6e^- \rightarrow xTi + (2-x)Fe + 6LiCN + 2H_2O$ and $2H_2O + 4Li + 4e^- \rightarrow H_2 + 2Li_2O$ (first discharge), and $Ti_x[Fe_{2-x}(CN)_6] + 6Li^+ + 6e^- \rightleftharpoons xTi + (2-x)Fe + 6LiCN$ (following cycles). The experiments performed by Piernas-Muñoz et al. [19] and Sun et al. [20] imply that the low voltage charge/discharge behavior is ascribed to Fe metal. Thus, the mechanism of the low voltage behavior is controversial even though the high reversible capacity and low voltage are promising. To clarify the mechanism, careful and systematic X-ray methods, such as XRD and X-ray absorption spectroscopy (XAS), are indispensable.

In this paper, we carefully investigated the low voltage charge/discharge behavior observed in the thin film of $Na_{1.34}Mn[Fe(CN)_6]_{0.84} \cdot 3.4H_2O$ (abbreviated as Mn-PBA) by means of ex situ synchrotron radiation XRD and XAS at Fe and Mn K edges without air exposure.

Our careful experiment revealed that the low voltage charge/discharge behavior has no relation to the Mn-PBA itself, but is ascribed to the byproducts, i.e., Fe and Mn metals, made by the reduction process of the Mn-PBA. We proposed that the low voltage behavior is mainly ascribed to the conversion reaction: $6e^- + Fe_2O_3 + 6Li^+ \rightleftharpoons 2Fe + 3\ Li_2O$.

2. Results

2.1. Scanning Electron Microscopy Image

Figure 1 shows SEM image of the as-grown and discharged films. The as-grown film consists of cubic particles of 1 μm in size, reflecting the face-centered cubic structure of Mn-PBA. The discharge process completely alters the particle shape. The discharged film consists of spherical particle of 0.5 μm in diameter. In addition, the color of the film changes from colorless (as-grown) to black (discharged). These observations suggest that the low voltage discharge process electrochemically decomposes Mn-PBA into another material. In other words, Mn-PBAs are just an initial reactant, and the resultant film (after the 1st discharge) is a porous film dispersed by Fe and Mn metals (vide infra).

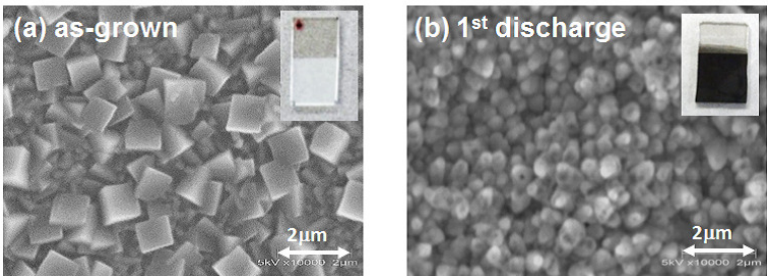

Figure 1. Scanning electron microscopy (SEM) images of (**a**) as-grown and (**b**) discharged films. Insets show pictures of the films.

2.2. Charge/Discharge Curves and Framework Structure

Figure 2a shows the charge/discharge curves of the Mn-PBA film in LIB. In the 1st discharge process, we observed irreversible capacity of 1400 mAh/g at voltage of 0.5 V. The capacity (=1400 mAh/g) of the 1st discharge process is slightly higher than those reported in literatures: 1000 mAh/g [16], 600 mAh/g [17], 1100 mAh/g [18], 1000 mAh/g [19], and 850 mAh/g [20]. The high irreversible capacity is probably ascribed to the thin film electrode and complete reduction reaction of PBA. After the 1st discharge process, reversible capacity of 370 mAh/g is observed. Figure 2c shows the XRD patterns of as-grown and discharged films in LIB. In the as-grown films, the all diffraction peaks can be indexed with face-centered cubic ($Fm\bar{3}m$: $Z = 4$) structure [21,22]. The lattice constant [a = 10.54267(13) Å] was refined by the Rietveld method (Rietan-FP [23]). In the discharged films, the diffraction peaks due to Mn-PBA completely disappear, indicating that the jungle-gym type network of PBA is completely destroyed. We, however, notice several weak additional peaks, suggesting formation of byproducts made by the reduction process of the Mn-PBA. The diffraction peaks due to Mn-PBA do not appear even in the 1st charged film. These observations indicate that the low voltage charge/discharge behavior has no relation to the Mn-PBA itself, but should be ascribed to the byproducts.

Figure 2c shows the charge/discharge curves of the Mn-PBA film in SIB. No detectable capacity is observed in the case of the larger Na^+, making a sharp contrast with the case of smaller Li^+. Figure 2d shows XRD patterns of as-grown and discharged films in SIB. The XRD pattern of the charge film is essentially the same as the as-grown film. The significant ion dependence suggests that the intercalation of smaller Li^+ causes the electrochemical decomposition of Mn-PBA.

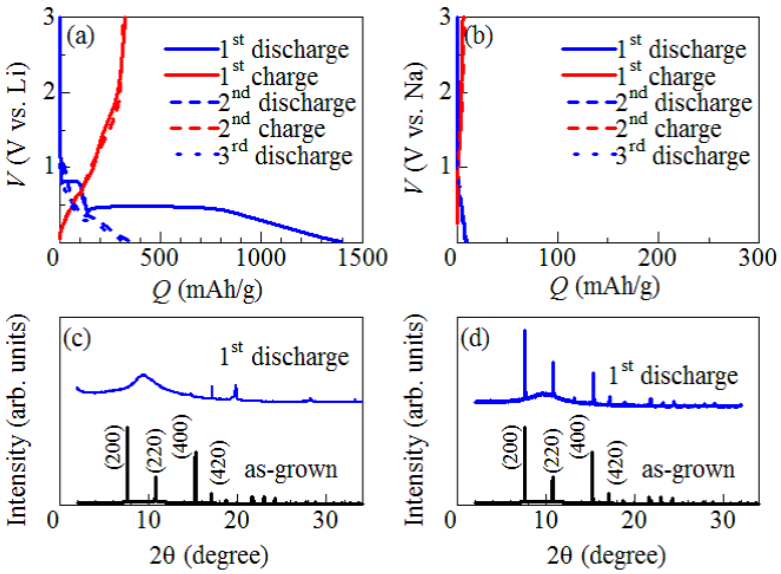

Figure 2. Charge/discharge curves of the Mn-PBA films against (**a**) Li and (**b**) Na; (**c**) X-ray diffraction (XRD) patterns of as-grown and discharged films in lithium-ion secondary battery (LIB); and (**d**) XRD patterns of the as-grown and discharged films in sodium-ion secondary battery (SIB). The wavelength of the incident X-ray was 0.69923 Å. The parentheses represents the index with face-centered cubic ($Fm\bar{3}m$: $Z = 4$) structure.

2.3. Synchrotron–Radiation X-ray Absorption Spectroscopy Measurement

Figure 3a shows X-ray absorption spectra of the discharged and charged films around the Fe K edges. The absorption edge of the charged film is the same as that of Fe metal (downward arrow), suggesting that Fe is reduced to metal after the discharge process. The spectral weight around the absorption edge significantly decreases in the charged film, suggesting that the Fe metal is oxidized

in the charge process. However, the overall spectral profile of the discharged and charged films seriously differs from that of Fe metal. In particular, peak structures are observed at 7122 eV in both the films, suggesting residual $[Fe(CN)_6]$ species [24,25]. We decomposed the Fe K edge spectra of the 1st discharge (Figure 3c) and 1st charge (Figure 3d) films into the spectra of the as-grown film, α-Fe_2O_3 and Fe metal. The decomposition suggests that the discharge film consists of 80% Fe metal and 20% $[Fe(CN)_6]$, while the charge film does 35% Fe metal, 45% α-Fe_2O_3, and 20% $[Fe(CN)_6]$. Thus, the XAS data clearly demonstrates that Fe metal is converted into α-Fe_2O_3 after the charge process. We note that the residual $[Fe(CN)_6]$ cannot contribute the redox reaction ($[Fe^{2+}(CN)_6]/[Fe^{3+}(CN)_6]$) in the charge/discharge process because the corresponding redox potential ($\approx$3.5 V versus Li/Li^+) is above the upper cut-off voltage (=3.0 V).

Figure 3b shows X-ray absorption spectra of the discharged and charged films around the Mn K edges. The absorption edge of the charged film is the same as that of Mn metal (downward arrow), suggesting that Mn is reduced to metal. We found that the spectral weight around the Mn K edge slightly decreases in the charged film. This suggests that a part of the Mn metal is oxidized after the charge process.

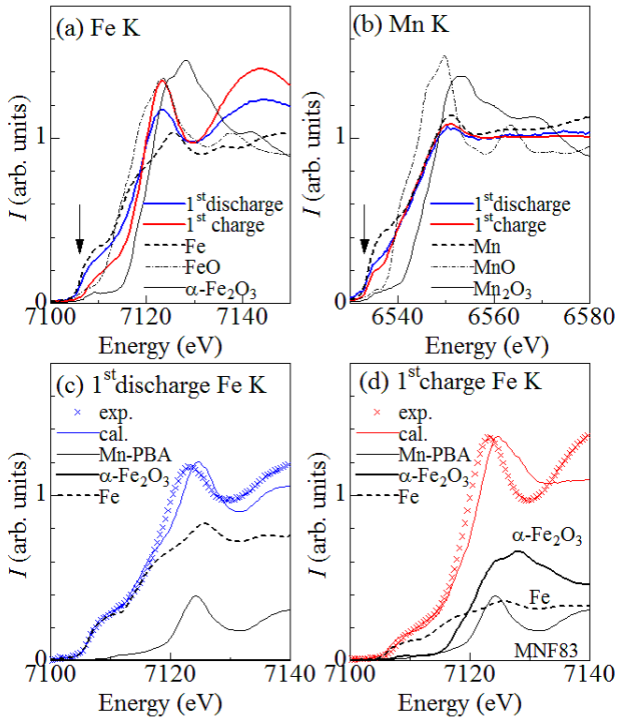

Figure 3. X-ray absorption spectra of discharged and charged films around the (**a**) Fe and (**b**) Mn K edges. The spectra of metal and oxides are also shown. Downward arrows indicate the absorption edge of the metal. Decomposition of Fe K edge spectra of (**c**) discharge and (**d**) charge films into the spectra of the as-grown film, α-Fe_2O_3 and Fe metal.

2.4. Synchrotron Radiation X-ray Diffraction Measurement

In order to specify the chemical products after the discharge and charge processes, we compared the observed XRD patterns with the simulated patterns of possible products, i.e., metals, oxides and hydrides. Figure 4a shows XRD patterns of the discharged film. All of the reflections can be ascribed to those of Fe metal (see the simulation at the bottom) except for the weak 34° reflection. Actually, the diffraction pattern of the experiment data is nearly the same as the simulation. Thus, we confirmed that the chemical product after the discharge process is Fe metal. It may be curious that no trace of Mn is discernible in the XRD pattern even though the XAS data suggest Mn metal. This is probably because the size of Mn metal is too small to be detected by XRD.

Figure 4b shows an XRD pattern of the charged film. Most of the reflections can be ascribed to those of α-Fe_2O_3 (see the simulation at the bottom). However, there exist other products such as β-Fe_2O_3, β-FeOOH and γ-FeOOH. The diffraction pattern seriously deviated from the simulation, probably due to the orientation effect of thin film.

Figure 4c shows cycle dependence of the intensities of the Fe peaks. The intensities decrease after the 1st charge process, increase after the 2nd discharge process, and then increase after the 2nd charge process. Figure 4d shows cycle dependence of the intensities of the α-Fe_2O_3 peaks. The intensities increase after the charge process and decrease after the discharge process. These cycle dependences clearly demonstrate reversible conversion reaction between Fe metal and α-Fe_2O_3.

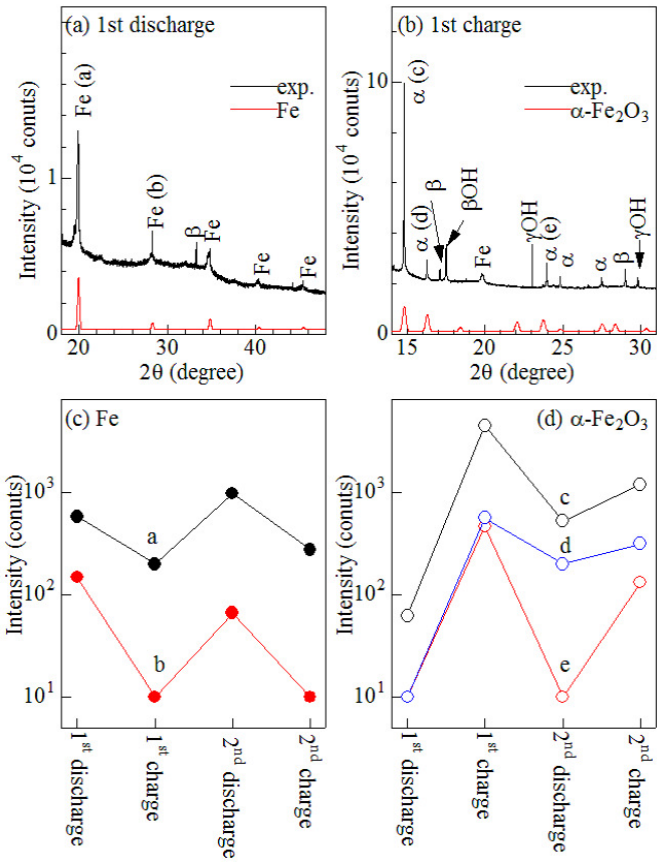

Figure 4. (**a**) XRD pattern of discharged film together with the simulated pattern of Fe; (**b**) XRD pattern of the charged film together with the simulated pattern of α-Fe_2O_3. Fe, α , β, βOH and γOH represent Fe metal, α-Fe_2O_3, β-Fe_2O_3. β-FeOOH and γ-FeOOH, respectively; (**c**) cycle dependence of the intensities of the Fe peaks; and (**d**) cycle dependence of the intensities of the α-Fe_2O_3 peaks.

3. Discussion

Now, let us propose a mechanism of the reversible low voltage charge/discharge behavior of Mn-PBA (see Figure 5). The XRD and XAS clearly demonstrate reversible conversion reaction between Fe metal and α-Fe_2O_3. Then, the most plausible chemical reaction is the conversion reaction of α-Fe_2O_3 [26]: $6e^- + Fe_2O_3 + 6Li^+ \rightleftharpoons 2Fe + 3Li_2O$. Here, we note that detection of Li_2O in the XRD pattern is difficult because the compound consists of only light elements. According to the electrochemical reaction, the ideal capacity of Mn-PBA is 260 mAh/g with use of the initial weight of Mn-PBA. The observed reversible discharge capacity (=370 mAh/g) is comparable but slightly higher than the ideal value (=260 mAh/g). The additional capacity is probably ascribed to the redox reaction of Mn metal, e.g., Mn/Mn^{2+} or Mn/Mn^{3+}. Actually, the spectral weight around the Mn K edge slightly decreases in the charged film (Figure 3b), suggesting that a part of the Mn metal is oxidized after the charge process.

Tarascon's group [27] reported the capacity of the conversion reaction of α-Fe_2O_3, whose size is 0.5 μm in diameter. However, the reversible discharge capacity (≈80 mAh/g) is much lower than the ideal value (=1007 mAh/g with use of the weight of α-Fe_2O_3). The high discharge capacity observed in our experiment may be ascribed to the nanoporous Fe metal state formed by the electrochemical decomposition process of Mn-PBA. We further investigated cycle properties of discharge capacity: 370 mAh/g at the 2nd, 301 mAh/g at the 4th, 260 mAh/g at the 6th, 200 mAh/g at the 8th, 120 mAh/g at the 10th, 70 mAh/g at the 12th, 40 mAh/g at the 14th, 30 mAh/g at the 16th, 20 mAh/g at the 18th, and 10 mAh/g at the 20th cycle. The rather poor cycle properties may be ascribed to the aggregation of the nanoparticle or surface degradation during the conversion process.

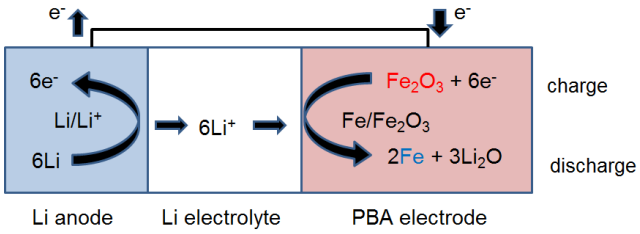

Figure 5. Schematic illustration for the reversible low voltage charge/discharge process. PBA: Prussian blue analogue.

4. Materials and Methods

4.1. Film Preparation and Characterization

Mn-PBA films were electrochemically synthesized on indium tin oxide (ITO) transparent electrodes under potentiostatic conditions at −0.45 V versus a standard Ag/AgCl electrode [5]. The electrolytes were aqueous solutions containing 1.0 mmol/L $K_3[Fe(CN)_6]$, 1.5 mmol/L $MnCl_2$, and 1 mol/L NaCl. The obtained film was colorless with a thickness of 1.5 μm. Before the film synthesis, the surface of the ITO electrode was purified by the electrolysis of water for 1 min. The chemical composition of the as-grown film is $Na_{1.34}Mn^{II}[Fe^{II}(CN)_6]_{0.84}\cdot 3.4H_2O$, which was determined by the inductively coupled plasma (ICP) method and CHN organic elementary analysis. Calculated: Na, 9.7; Mn, 16.9; Fe, 14.5; C, 18.7; H, 2.1; N, 21.8%. Found: Na, 10.06; Mn, 16.8; Fe, 14.7; C, 18.2; H, 2.1; N, 20.9%. Please define or full spell the acronym for its first appearance, if possible. The mass of each film was evaluated from the film thickness of the experimentally determined film density (71% of the ideal density). The morphologies of the films were investigated by SEM images using Mighty-8 (TECHNEX Mighty-8, Tokyo, Japan). The acceleration voltage was 2 keV.

4.2. X-ray Diffraction and X-ray Absorption Spectroscopy

The XRD pattern of the Mn-PBA films were obtained using the synchrotron radiation X-ray source at the BL02B2 beamline [28] of SPring-8. The films were carefully removed by a microspatula in an Ar-filled grove box. The powders were filled into ϕ = 0.3-mm borosilicate capillaries without air exposure and were placed on a Debye–Scherrer camera. The exposure time was 10 min. The X-ray wavelength (=0.69923 Å) was calibrated using the lattice constant of standard CeO_2 powder.

To investigate the valence state of Fe and Mn, XAS was performed at the BL01B1 beamline of SPring-8 in a transmission configuration. In the XAS measurements, we used the same powder samples filled in ϕ = 0.3-mm borosilicate capillaries. The background subtraction and normalization were done using the ATHENA program [29].

4.3. Electrochemical Measurement

The electrochemical measurements were carried out with potentiostat (HokutoDENKO HJ1001SD8, Tokyo, Japan) in an Ar-filled glove box using a beaker-type cell. In the LIB, the cathode,

anode, and electrolyte were the thin film, ethylene carbonate (EC)/diethyl carbonate (DEC) solution containing 1 mol/L $LiClO_4$, and Li metal, respectively. The charge/discharge current density was 25 $\mu A/cm^2$. The lower and upper cut-off voltages were 0.01 and 3.0 V, respectively. In the SIB, the cathode, anode, and electrolyte were the thin film propylene carbonate (PC) solution containing 1 mol/L $NaClO_4$, and Na metal, respectively. The active area was 2.0 cm^2. The charge/discharge current density was 4.8 $\mu A/cm^2$. The lower and upper cut-off voltages were 0.01 and 3.0 V, respectively. We note that the as-grown Mn-PBA film shows Li^+/Na^+ deintercalation [5,8] at ≈3.5 V versus Li/Li^+ and ≈3.3 V versus Na/Na^+. These redox potentials are above the upper cut-off voltage (=3.0 V), and, hence, the Mn-PBA does not show Li^+/Na^+ deintercalation.

5. Conclusions

We performed ex situ synchrotron radiation XRD and XAS measurements of a film of $Na_{1.34}Mn[Fe(CN)_6]_{0.84}\cdot 3.4H_2O$ without air exposure. Based on the careful analyses of the XRD and XAS data, we proposed that the low voltage behavior of the Mn-PBA film is mainly ascribed to a conversion reaction: $6e^- + Fe_2O_3 + 6Li^+ \rightleftharpoons 2Fe + 3Li_2O$. Thus, the careful electrochemical experiment combined with the XRD and XAS analysis revealed that the low voltage charge/discharge behavior has no relation to the Mn-PBA itself, but is ascribed to the byproduct, i.e., Fe and Mn metals, made by the reduction process of the Mn-PBA. It is dangerous to rely only on electrochemical measurements for PBA studies because it misled us into regarding the low voltage properties of PBA.

Acknowledgments: This work was supported by the Yazaki Memorial Foundation for Science and Technology, Tokyo, Japan and the Nippon Sheet Glass Foundation for Materials Science and Engineering, Tokyo, Japan. We appreciated Shota Urase for his help in the initial stage of this work. Takayuki Shibata was supported by the Nanotech Research Professional (NRP) course of the Nanotech Career-Up Alliance in Nanotech (CUPAL) project. The XRD measurements were performed using the BL02B2 beamlines (Proposal No. 2015B1077) of SPring-8 with the approval of the Japan Synchrotron Radiation Research Institute (JASRI), Hogo, Japan. The XAS measurements were performed using the BL01B1 beamlines (Proposal No. 2015B1076) of SPring-8 with the approval of the Japan Synchrotron Radiation Research Institute (JASRI). The elementary analyses were performed at the Chemical Analysis Division, Research Facility Center for Science and Engineering, University of Tsukuba, Tsukuba, Japan.

Author Contributions: Takayuki Shibata performed all the experiments including the film preparation, characterization, electrochemical procedure, synchrotron radiation XRD, and XAS measurements. Masamitsu Takachi provided advice regarding the film preparation and characterization. Yutaka Moritomo planned the research and wrote the manuscript.

Conflicts of Interest: The authors declare no conflict of interest.

References

1. Kitagawa, S.; Kitaura, R.; Noro, S. Functional porous coordination polymers. *Angew. Chem. Int. Ed.* **2004**, *43*, 2334–2375.
2. Imanishi, N.; Morikawa, T.; Kondo, J.; Takeda, Y.; Yamamoto, O.; Kinugasa, N.; Yamagishi, T. Lithium intercalation behavior into iron cyanide complex as positive electrode of lithium secondary battery. *J. Power Sources* **1999**, *79*, 215–219.
3. Imanishi, N.; Morikawa, T.; Kondo, J.; Yamane, R.; Takeda, Y.; Yamamoto, O.; Sakaebe, H.; Tabuchi, M. Lithium intercalation behavior of iron cyanometallates. *J. Power Sources* **1999**, *81–82*, 530–534.
4. Okubo, M.; Asakura, D.; Mizuno, Y.; Kim, J.-D.; Mizokawa, T.; Kudo, T.; Honnma, I. Switching redox-active sites by valence tautomerism in Prussian blue analogues $A_xMn_y[Fe(CN)_6]\cdot nH_2O$ (*A*: K, Rb): Robust frameworks for reversible Li storage. *J. Phys. Chem. Lett.* **2010**, *1*, 2063–2071.
5. Matsuda, T.; Moritomo, Y. Thin film electrode of Prussian blue analogue for Li-ion battery. *Appl. Phys. Express* **2011**, *4*, 047101.
6. Takachi, M.; Matsuda, T.; Moritomo, Y. Structural, electronic, and electrochemical properties of $Li_xCo[Fe(CN)_6]_{0.90}\cdot 2.9H_2O$. *Jpn. J. Appl. Phys.* **2013**, *52*, 044301.
7. Lu, Y.; Wang, L.; Cheng, J.; Goodenough, J.B. Prussian blue: A new framework of electrode materials for sodium batteries. *Chem. Commun.* **2012**, *48*, 6544–6546.

8. Matsuda, T.; Takachi, M.; Moritomo, Y. A sodium manganese ferrocyanide thin film for Na-ion batteries. *Chem. Commun.* **2013**, *49*, 2750–2752.
9. Takachi, M.; Matsuda, T.; Moritomo, Y. Cobalt hexacyanoferrate as cathode material for Na^+ secondary battery. *Appl. Phys. Express* **2013**, *6*, 025802.
10. Yang, D.; Xu, J.; Liao, X.-Z.; He, Y.-S.; Liu, H.; Ma, Z.-F. Structure optimization of Prussian blue analogue cathode materials for advanced sodium ion batteries. *Chem. Commum.* **2014**, *50*, 13377–13380.
11. Moritomo, Y.; Urase, S.; Shibata, T. Enhanced battery performance in manganese hexacyanoferrate by partial substitution. *Electrochim. Acta* **2016**, *210*, 963–969.
12. Lee, H.W.; Wang, R.Y.; Pasta, M.; Lee, S.W.; Liu, N.; Chi, Y. Manganese hexacyanomanganate open framework as a high-capacity positive electrode material for sodium-ion batteries. *Nat. Commun.* **2014**, *5*, 5280.
13. Wang, L.; Song, J.; Qiao, R.; Wray, L.A.; Hossain, M.A.; Chung, Y.-D.; Yang, W.; Lu, Y.; Evans, D.; Lee, J.-J.; et al. Rhombohedral Prussian white as cathode for rechargeable sodium-ion batteries. *J. Am. Chem. Soc.* **2015**, *137*, 2548–2554.
14. Buser, H.J.; Schwarzenbach, D.; Petter, W.; Ludi, A. The crystal structure of Prussian blue: $Fe_4[Fe(CN)_6]_3 \cdot xH_2O$. *Inorg. Chem.* **1997**, *16*, 2704–2710.
15. Herren, F.; Fischer, P.; Ludi, A.; Halg, W. Neutron diffraction study of Prussian blue, $Fe_4[Fe(CN)_6]_3 \cdot xH_2O$. Location of water molecules and long-range magnetic order. *Inorg. Chem.* **1980**, *19*, 956–959.
16. Shokouhimehr, M.; Yu, S.-H.; Lee, D.-C.; Ling, D.; Hyeon, T.; Sung, Y.-E. Metal hexacyanoferrate nanoparticles as electrode materials for lithium ion batteries. *Nanosci. Nanotechnol. Lett.* **2013**, *5*, 770–774.
17. Nie, P.; Shen, L.; Luo, H.; Ding, B.; Xu, G.; Wang, J. Prussian blue analogues: A new class of anode materials for lithium ion batteries. *J. Mater. Chem. A* **2014**, *2*, 5852–5857.
18. Xiong, P.; Zeng, G.; Zeng, L.; Wei, M. Prussian blue analogues $Mn[Fe(CN)_6]_{0.6667} \cdot nH_2O$ cubes as an anode material for lithium-ion batteries. *Dalton Trans.* **2015**, *44*, 16746–16751.
19. Piernas-Muñoz, M.J.; Castillo-Martínez, E.; Roddatis, V.; Armand, M.; Rojo, T. $K_{1-x}Fe_{2+x/3}(CN)_6 \cdot yH_2O$, Prussian blue as a displacement anode for lithium ion batteries. *J. Power Sources* **2014**, *271*, 489–496.
20. Sun, X.; Ji, X.-Y.; Zhou, Y.-T.; Shao, Y.; Zang, Y.; Wen, Z.-Y.; Chen, C.-H. A new gridding cyanoferrate anode material for lithium and sodium ion batteries: $Ti_{0.75}Fe_{0.25}[Fe(CN)_6]_{0.96} \cdot 1.9H_2O$ with excellent electrochemical properties. *J. Power Sources* **2016**, *314*, 35–38.
21. Moritomo, Y.; Kurihara, Y.; Matsuda, T.; Kim, J. Structural phase diagram of Mn-Fe cyanide against cation concentration. *J. Phys. Soc. Jpn.* **2011**, *80*, 103601.
22. Moritomo, Y.; Matsuda, T.; Kurihara, Y.; Kim, J. Cubic-rhombohedral structural phase transition in $Na_{1.32}Mn[Fe(CN)_6]_{0.83} \cdot 3.6H_2O$. *J. Phys. Soc. Jpn.* **2011**, *80*, 074608.
23. Izumi, F.; Momma, K. Three-dimensional visualization in powder diffraction. *Solid State Phenom.* **2007**, *130*, 15–20.
24. Bianconi, A.; Dell'Ariccia, M.; Durham, P.J.; Pendry, J.B. Multiple-scattering resonances and structural effects in the X-ray-absorption near-edge spectra of Fe II and Fe III hexacyanide complexes. *Phys. Rev. B* **1982**, *26*, 6502–6508.
25. Hayashi, H.; Abe, H. X-ray spectroscopic analysis of liesegang patterns in Mn-Fe-based Prussian blue analogs. *J. Anal. At. Spectrom.* **2016**, *31*, 1658–1672.
26. Li, H.; Balaya, P.; Maier, J. Li-storage via heterogeneous reaction in selected binary metal fluorides and oxides. *J. Electrochem. Soc.* **2004**, *151*, A1878–A1885.
27. Larcher, D.; Masquelier, C.; Bonnin, D.; Chabre, Y.; Masson, V.; Leriche, J.-B.; Tarascon, J.-M. Effect of particle size on lithium intercalation into α-Fe_2O_3. *J. Electrochem. Soc.* **2003**, *150*, A133–A139.
28. Nishibori, E.; Takata, M.; Kato, K.; Sakata, M.; Kubota, Y.; Aoyagi, S.; Kuroiwa, Y.; Yamakawa, M.; Ikeda, N. The large Debye-Scherrer camera installed at SPring-8 Bl02B2 for charge density studies. *J. Phys. Chem. Solids* **2001**, *62*, 2095–2098.
29. Ravel, B.; Newville, M. ATHENA, ARTEMIS, HEPHAESTUS: Data analysis for X-ray absorption spectroscopy using IFEFFIT. *J. Synchrotron Radiat.* **2005**, *12*, 537–541.